Inorganic Chemistry
Article
Cite This: Inorg. Chem. XXXX, XXX, XXX−XXX
pubs.acs.org/IC

Combining Experiments and Theoretical Modeling To Interrogate the Anisotropic Growth and Structure−Plasmonic Property Relationships of Gold Nanostars

Haitao Wang,[†] Yuhan Pu,[†] Beibei Shan, and Ming Li*

School of Materials Science and Engineering, State Key Laboratory for Power Metallurgy, Central South University, Changsha, Hunan 410083, China

Supporting Information

ABSTRACT: We present a combined strategy of experiments and theoretical modeling for understanding the evolution of the morphology and plasmonic properties of gold nanostars (GNSs) in the seed-mediated synthesis by changing the poly(vinylpyrrolidone) (PVP) molecular weight, PVP concentration, and synthesis temperature. A dramatic change of the morphology of GNSs as a function of these synthesis parameters is observed that is related to variations of the plasmonic properties and thus surface-enhanced Raman spectroscopy (SERS) enhancement. We observe the favorable growth of anisotropic GNS structures with sharp protruding tips using PVP of low molecular weight and of rounded GNSs with short protruding tips using PVP of high molecular weight. The PVP concentration has less influence on the core size than on the tip length of GNSs. The high synthesis temperature causes the rounding of the GNS structure. Finite-difference time-domain (FDTD) simulations reveal a remarkable correlation of the GNS morphology with the plasmonic properties as well as the SERS enhancement. The maximum local electric field enhancement occurs at the apex of the sharp protruding tips of the GNSs. The weak plasmonic coupling is observed between the protruding tips of GNSs because of their large separation distance, and increasing the number of protruding tips beyond two only increases the extinction cross section without further red-shifting the plasmon peak. A resonance overlap of the plasmon band with the incident laser wavelength is responsible for the morphology-dependent plasmonic properties and SERS enhancement. The present work demonstrates that a mechanistic understanding of the structural evolution of GNSs along with their morphology−plasmonic property correlation can be achieved through the combination of experimental investigations and FDTD-based theoretical modeling.

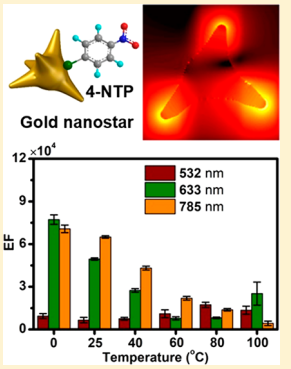

1. INTRODUCTION

Plasmonic gold nanostars (GNSs) have opened up exciting opportunities in various fields of plasmon-enhanced spectroscopy, biosensing, catalysis, solar energy harvesting, nanolasers, nanooptics, and phototheranostics.[1−3] These GNSs of anisotropic structural and optical properties typically consist of a central core and multiple protruding tips distributed on the central core. Local confinement of the electromagnetic field at the sharp tips of GNSs arising from the so-called localized surface plasmon resonance effects enables tremendous electromagnetic enhancement, forming "hot spots" for the enhancement of numerous optical phenomena.[4−8] In addition, the protruding tips asymmetrically distributed on the central core offer a broad tuning flexibility of plasmon wavelengths in the visible and near-infrared (NIR) spectral regions, which is of great significance for biomedical applications.[2] GNSs typically possess two characteristic plasmon bands in the short- and long-wavelength regions of their extinction spectra, which originate from hybridization of the core- and protruding-tip-associated plasmons.[9,10] The fascinating morphology of GNSs is responsible for their unique plasmonic properties for exciting plasmonic applications. The position, intensity, and line width of plasmon bands of GNSs are directly linked to the particle size, morphology, refractive index of surrounding media, and interparticle interactions.[9,11−13] More specifically, the plasmon features of GNSs can be finely tuned by varying the dimensions of the central core as well as the number, length, and aspect ratio of the protruding tips. Thus, GNSs have become the prominent plasmonic materials with tunable plasmon bands in the visible−NIR region and remarkable confinement of the plasmonic fields.[11] However, the morphology of GNSs is quite complex so that the correlation of the morphology with the plasmon features has yet to be completely established so far.

A systematic study of the morphology−plasmon relationship of GNSs requires the synthesis of high-quality GNSs with well-defined geometry and will eventually strengthen our understanding of their growth mechanism and corresponding plasmonic properties. While few seedless methods have been developed for the synthesis of GNSs,[14,15] the seed-mediated synthetic method using gold seeds of various sizes and shapes has been widely adopted because of its high yield, high monodispersity, and operation simplicity.[5,9,11,16−20] The seed-mediated synthesis of GNSs is based on the temporal separation of nucleation and growth for better controllability

Received: July 22, 2019

DOI: 10.1021/acs.inorgchem.9b02187
Inorg. Chem. XXXX, XXX, XXX−XXX

and typically performed in an *N*,*N*-dimethylformamide (DMF) solution of poly(vinylpyrrolidone) (PVP). The amphiphilic PVP molecules can serve multiple functions such as a surface stabilizer, a shape-directing agent, a dispersant, and a reducing agent.[21,22] The gold−PVP interaction occurs through either the carbonyl group or nitrogen atom of the pyrrolidone ring, and the selective adsorption of PVP onto the low-energy Au{111} crystal facets induces the favorable deposition of reduced gold atoms, thereby producing the anisotropic GNS structure.[21,23] Intensive efforts have been made to improve the seed-mediated synthesis of GNSs, achieving high-quality, monodisperse GNSs and better control over their specific morphology and plasmonic properties.[5,9,11,16−20,24−28] We previously investigated the seed-mediated growth process of GNSs with tailorable core size and tip dimensions by varying the gold seed concentration and demonstrated the structure-dependent plasmonic properties. The gold seed concentration not only affects the core size and tip dimensions but also leads to significant changes in the structure heterogeneity of GNSs.[9] Although Khoury and Vo-Dinh correlated the overall size of the GNSs with the surface-enhanced Raman spectroscopy (SERS) performance through a systematic analysis of the feature of the protruding tips of GNSs synthesized by various concentrations of gold seeds, they did not clarify how the overall size affected the plasmon resonance of the GNSs and the corresponding electric-field distribution.[13] Actually, not only the overall size of the GNSs but also the core size, tip number, and tip length are more critical for the plasmonic properties and resultant SERS enhancement. A full understanding of the effects of other experimental variables such as the PVP molecular weight, PVP concentration, and synthesis temperature on the seed-mediated growth of GNSs is still lacking. The hybridization model of the GNSs was proposed by Nordlander and co-workers, but the effects of dimensional parameters (e.g., core size, tip number, and tip length) on the plasmonic properties are still unclear.[10] Furthermore, the increasing use of GNSs over diverse fields has created growing demand for establishing their morphology−plasmon relationships describing the corresponding plasmonic behaviors.

In the present work, we systematically investigated the seed-mediated synthesis of GNSs under varying reaction conditions such as the PVP molecular weight, PVP concentration, and synthesis temperature. The combination of experimental investigations with finite-difference time-domain (FDTD)-based theoretical modeling allows not only the study of the evolution of dimensional parameters with these reaction conditions but also clarification of the correlation of the plasmonic property with these dimensional parameters, which is unachievable by experiments alone. Experimentally, we chose the PVP oligomers of different molecular weights for both gold seed coating and GNS growth and further investigated the effects of the PVP concentration and synthesis temperature on the morphology of GNSs. Our results showed dramatic changes of the morphology and resultant plasmon features of GNSs by varying these synthesis conditions. Achieving GNSs of various core sizes and tip lengths allows us to interrogate the structure−plasmonic property relationship by combining the experimental results with FDTD simulations. Following this, we examined the structure−plasmon-dependent SERS enhancement under different incident lasers. Our work represents significant advancement of the understanding of the seed-mediated growth of GNSs and thereby provides fundamental insight into their structure−plasmonic property correlations. We believe that this work will benefit not only the synthesis of high-quality of GNSs but also the implementation of these GNSs in diverse fields for practical applications.

2. EXPERIMENTAL SECTION

2.1. Chemicals and Materials. Trisodium citrate dihydrate [$HOC(COONa)(CH_2COONa)_2{\cdot}2H_2O$, analytical reagent] and poly(vinylpyrrolidone) (PVP) oligomers of various molecular weights (PVP-8, PVP-10, PVP-24, PVP-40, and PVP-58 denote PVPs of molecular weights of 8000, 10000, 24000, 40000, and 58000, respectively) were purchased from Sigma-Aldrich Shanghai Trading Co., Ltd. (Shanghai, China). Chloroauric acid ($HAuCl_4{\cdot}4H_2O$; 99% trace metals basis) was purchased from Shanghai Civi Chemical Technology Co., Ltd. (Shanghai, China). Sodium borohydride ($NaBH_4$; ≥98%) and *N*,*N*-dimethylformamide (DMF; anhydrous 99.8%) were purchased from Sinopharm (Beijing, China). 4-Nitrobenzenethiol (4-NTP; 90%) was purchased from Shanghai Macklin Biochemical Co., Ltd. (Shanghai, China). Anhydrous ethanol (≥99.7%) was purchased from Nanjing Chemical Reagent Co., Ltd. (Nanjing, China). Ultrapure water was produced by a Millipore Direct-Q3 UV system (18.2 MΩ·cm at 25 °C) (Millipore Corp., Molshein, France). All chemicals were used as received, and all glassware was cleaned with aqua regia and then air-dried before use throughout the experiments.

2.2. Synthesis of PVP-Coated Gold Seeds. First, 1 mL of a 1 wt % $HAuCl_4{\cdot}4H_2O$ aqueous solution was diluted to 90 mL with the addition of ultrapure water, followed by the immediate injection of 2 mL of a 38.8 mM trisodium citrate aqueous solution. Then, 1 mL of a freshly prepared trisodium citrate solution (38.8 mM) containing 0.075 wt % $NaBH_4$ was added dropwise within 5 min. The gold seed solution was achieved after constant stirring overnight at room temperature. Finally, PVPs of various molecular weights (PVP-8, PVP-10, PVP-24, PVP-40, or PVP-58) were added with a final concentration of 10 mM. Followed by stirring for 24 h at room temperature, PVP-coated gold seeds were obtained with a final concentration of 0.58 nM, measured by UV−visible extinction spectroscopy, the details of which can be found in the literature published by our group.[9]

2.3. Synthesis of GNSs. GNSs were synthesized using PVPs of different molecular weights at a given temperature according to the seed-mediated growth method reported in our previous work with a slight modification.[5,9,11,20,29−33] To assess the effect of the PVP molecular weight on the synthesis of GNSs, 27 μL of a 20 mM $HAuCl_4{\cdot}4H_2O$ aqueous solution was added to a DMF solution of 5.0 mM PVP (PVP-8, PVP-10, PVP-24, PVP-40, or PVP-58), followed by the addition of 29 μL of a gold seed aqueous solution coated by the corresponding PVP. The reaction was continued for 3 h at 25 °C and then washed with ethanol and ultrapure water at least three times. The pellets were the resultant GNSs synthesized by PVP-8, PVP-10, PVP-24, PVP-40, or PVP-58, which were redispersed in 1 mL of ultrapure water for further use.

To investigate the effect of the PVP concentration, we chose PVP-10 for the synthesis of GNSs. The synthetic process was the same as that described above except that the PVP-10 concentration was changed to 2.0, 2.5, 10.0, 15.0, or 20.0 mM. To examine the effect of the synthesis temperature, the synthesis temperature was set to 0, 25, 40, 60, 80, or 100 °C, while all other synthesis conditions were kept constant. All as-prepared GNSs were stored in ultrapure water for further use.

2.4. Characterization. Optical extinction spectra were recorded using an Agilent Cary 5000 UV−visible−NIR spectrophotometer (Agilent Technologies, Inc., Santa Clara, CA). Transmission electron microscopy (TEM) images were collected with a Tecnai G2 F20 transmission electron microscope (FEI Inc., Hillsboro, OR) operating at an accelerating voltage of 200 kV for observation of the morphology of GNSs. All samples were successively centrifuged and washed with ultrapure water before dropping it onto a thin carbon-coated 300 mesh copper grid (Beijing Zhongjingkeyi Technology Co.,

DOI: 10.1021/acs.inorgchem.9b02187
Inorg. Chem. XXXX, XXX, XXX−XXX

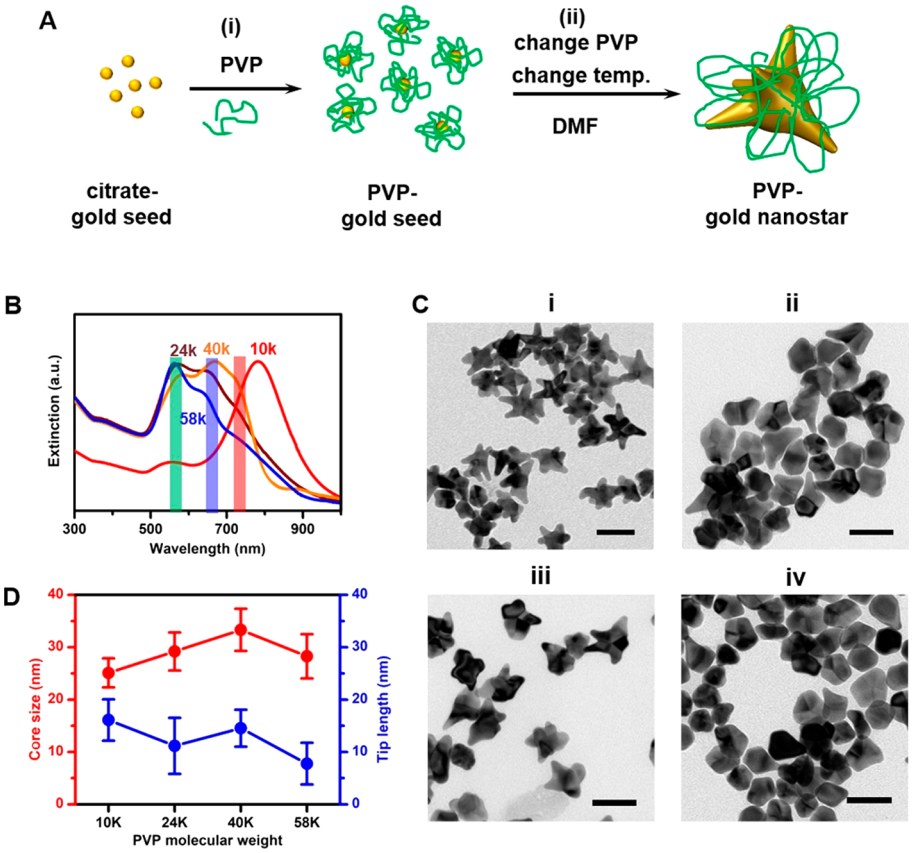

Figure 1. Effect of the PVP molecular weight on the synthesis of GNSs. (A) Schematic describing the seed-mediated synthesis process of GNSs, which involves two separate steps: (i) synthesis of PVP-coated gold seeds and (ii) anisotropic growth of GNSs. (B) Extinction spectra and (C) representative TEM images of GNSs synthesized using (i) PVP-10, (ii) PVP-24, (iii) PVP-40, and (iv) PVP-58. Marked regions in part B indicate three distinct plasmon bands of GNSs synthesized using PVP-24, PVP-40, and PVP-58. (D) Core size and tip length as a function of the PVP molecular weight, statistically obtained from the TEM data. Scale bar: 50 nm.

Ltd., Beijing, China). Dimensional parameters of GNSs were statistically determined from the TEM data using the *ImageJ* analysis software. More than 100 particles were measured and analyzed for each type of nanoparticle. To minimize the measurement error of the tip length of GNSs, we assume that all protruding tips have the same length and use the largest tip length in the TEM images to represent the tip length in the 3D GNSs.

2.5. SERS Measurements. Both Raman spectroscopy and SERS measurements were performed on a Renishaw inVia Raman microscope system equipped with a Leica DM2700 M Ren RL/TL microscope and two Peltier-cooled CCD array detectors with two gratings of 1200 and 1800 lines mm^{-1}. Raman or SERS spectra were collected using three lasers of different excitation wavelengths at 532, 633, and 785 nm through a 5× (N.A. 0.12) Leica objective fitted with filters to exclude signals from the laser and Rayleigh scatterings. For SERS sample preparation, 4-NTP molecules (300 nM) were incubated with the GNS suspension. After stirring for 1 h and then standing for ~24 h at room temperature, the reaction mixture was washed three times with ultrapure water to remove excess free 4-NTP molecules. The resultant pellets were 4-NTP-modified GNSs, dispersed in 0.5 mL of ultrapure water for the following measurements. For normal Raman or SERS measurements, an aliquot of a 4-NTP solution or a 4-NTP-modified GNS suspension was exposed to the laser power of 2.6 mW for 532 nm, 0.9 mW for 633 nm, or 2.0 mW for 785 nm incident lasers, and 1 s of exposure time and one scan accumulation were adopted. At least 20 SERS spectra were collected at different positions for each type of sample and averaged to attain the representative SERS response.

The SERS enhancement factor (EF) was estimated using the following equation:[34,35]

$$\mathrm{EF} = \frac{I_{\mathrm{SERS}}/N_{\mathrm{ads}}}{I_{\mathrm{Raman}}/N_{\mathrm{vol}}} \quad (1)$$

where I_{SERS} is the SERS peak intensity of the 4-NTP molecules adsorbed onto the GNSs, I_{Raman} is the Raman peak intensity of a 4-NTP bulky solution in the absence of GNSs, N_{ads} is the number of 4-NTP molecules adsorbed on the GNSs, which is introduced in detail in the Supporting Information, and N_{vol} is the number of 4-NTP molecules in the focal volume of the incident lasers in the absence of GNSs. To calculate N_{vol}, the following equation was used:

$$N_{\mathrm{vol}} = C_{\mathrm{RS}}V \quad (2)$$

where C_{RS} is the bulky concentration of a 4-NTP solution and V is the focal volume of the focused incident lasers, depending on the laser wavelength.

2.6. FDTD Simulations. Both extinction spectra and electromagnetic field distribution were calculated using the commercial software *Lumerical FDTD Solutions 8.6* (Lumerical Solutions Inc., Vancouver, Canada). The model of gold nanostructures was created using an *AutoCAD* software based on the dimensional parameters (core size, tip length, and number) statistically obtained from the TEM data. The dielectric function of gold was taken from the measured data of Johnson and Christy.[36] The background refractive index of the surrounding medium (water) was set as 1.33. The mesh size of the GNS and its surrounding space was 0.5 nm, and the sharp tip area was meshed into 0.1 nm. A total-field scattered field was used as the input source.

The theoretical molar extinction coefficients ($\varepsilon_{\mathrm{FDTD}}$) can be calculated through the extinction cross sections (σ_{ext}) obtained from the FDTD simulations using the following equation:[37]

DOI: 10.1021/acs.inorgchem.9b02187
Inorg. Chem. XXXX, XXX, XXX−XXX

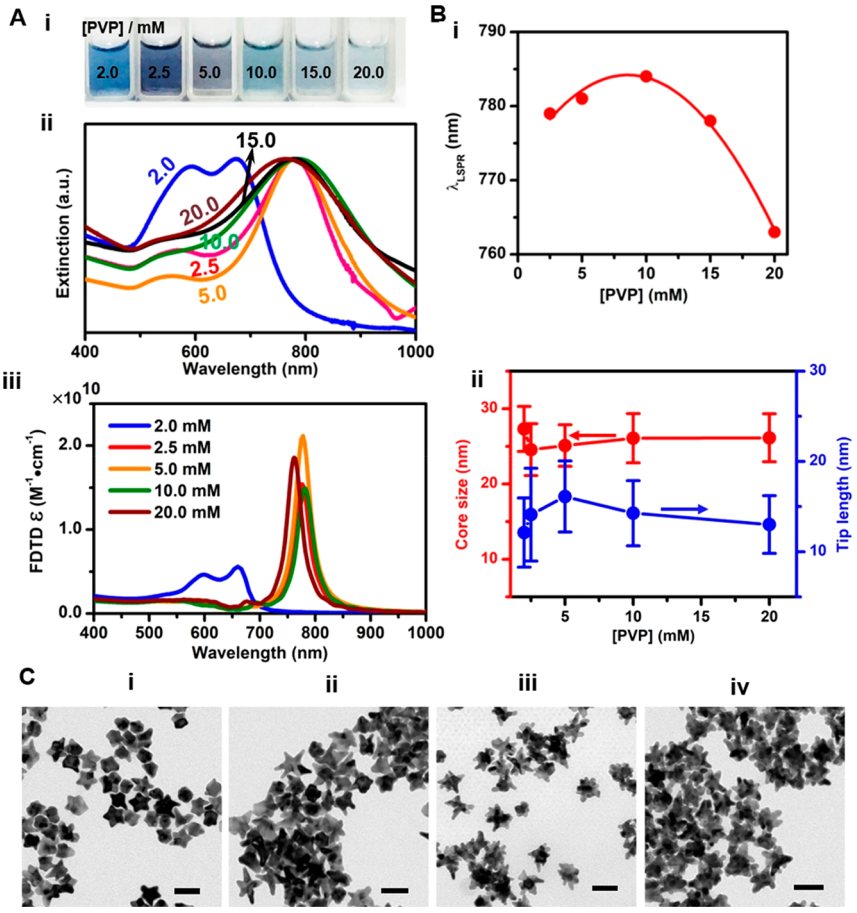

Figure 2. Effect of the PVP concentration on the synthesis of GNSs. (A) (i) Optical images, (ii) experimental extinction spectra, and (iii) calculated extinction spectra of GNSs obtained with varying PVP-10 concentrations: 2.0, 2.5, 5.0, 10.0, 15.0, and 20.0 mM. (B) (i) Plasmon wavelength and (ii) core size and tip length of GNSs as a function of the PVP concentration. (C) TEM images of GNSs obtained at the PVP-10 concentration of (i) 2.0, (ii) 2.5, (iii) 10.0, and (iv) 20.0 mM. Scale bar: 50 nm.

$$\varepsilon_{\mathrm{FDTD}} = \frac{N_{\mathrm{A}}}{2.3 \times 10^{3}} \sigma_{\mathrm{ext}} (\mathrm{M}^{-1}\,\mathrm{cm}^{-1}) \tag{3}$$

where N_{A} is Avogadro's number.

3. RESULTS AND DISCUSSION

3.1. Effects of the Molecular Weight and Concentration of PVP. The seed-mediated synthetic protocol of GNSs typically involves two separate steps: the synthesis of PVP-coated gold seeds and anisotropic growth of GNSs (Figure 1A).[5,9,11,20,29−33] The small gold seeds were first synthesized by reducing Au^{3+} ions with $NaBH_4$ in the presence of trisodium citrate, followed by ligand exchange with PVP to yield PVP-coated gold seeds. Then, growth of GNSs was performed using PVP-coated gold seeds in a DMF solution of PVP. DMF serves as the reducing agent of Au^{3+} to Au^{+}, as demonstrated by the complete disappearance of the light-yellow color after the immediate addition of the Au^{3+} precursor.[9,38] Two critical roles of PVP in the synthesis of GNSs are to reduce Au^{+} to Au^{0} and to induce the anisotropic deposition of Au^{0} atoms on the gold seed surface.[21,22] The favorable adsorption of PVP on the Au{111} facets inhibits the deposition of Au^{0} atoms along the ⟨111⟩ direction and consequentially induces anisotropic growth to produce the GNS structure.[9,21]

To assess the effect of the PVP molecular weight, PVP-8, PVP-10, PVP-24, PVP-40, and PVP-58 were chosen for the synthesis of GNSs, which represent PVP oligomers with molecular weights of 8, 10, 24, 40, and 58 kg mol^{-1}, respectively. Extinction spectra exhibit two characteristic plasmon bands at 558 and 780 nm for PVP-10-synthesized GNSs; three plasmon bands at 550−600, 650−690, and ∼750 nm are clearly observed in all extinction spectra of PVP-24-, PVP-40-, and PVP-58-synthesized GNSs (Figure 1B). The main plasmon mode at the long wavelength is dominant in the extinction spectrum of PVP-10-synthesized GNSs, while the two plasmon bands in the short-wavelength region are much stronger in all three other GNSs. We did not observe the color change to blue (or any other color) when PVP-8 was used, indicating no formation of GNSs. TEM images show dramatic changes of the morphology of these gold nanostructures with the use of PVPs of different molecular weights (Figure 1C). There exist about five sharp tips in a single GNS synthesized with PVP-10, but these tips become rounded more or less in the cases of PVP-24, PVP-40, and PVP-58. The statistical analysis from TEM images reveals that the core size of GNSs first increases and then decreases as the molecular weight increases, with the biggest core size achieved when PVP-40 was used; the tip length roughly decreases with increasing PVP molecular weight (Figures 1D and S2). As aforementioned, PVP works as a reducing agent in the seed-mediated synthesis of GNSs. However, the reducing power of PVP significantly affects the kinetics of nucleation and then the anisotropic growth of GNSs.[39] PVP with high molecular weight typically

DOI: 10.1021/acs.inorgchem.9b02187
Inorg. Chem. XXXX, XXX, XXX−XXX

comprises a much larger number of monomers, which have more reducing active sites for the enhanced reducing power, as shown in the literature.[39] In addition, PVP with high molecular weight yields high steric hindrance for the stability of PVP toward the gold surface and accordingly inhibits the anisotropic growth of GNSs. The reducing power of PVP for Au^+ to Au^0 increases and the stabilization ability decreases as a result of steric hindrance with increasing molecular weight.[40,41] High-quality GNSs with sharp protruding tips are achievable using PVP-10, although PVP-24, PVP-40, and PVP-58 of high reducing power enable the fast reduction of Au^+ to Au^0 and their high steric hindrance inhibits the anisotropic deposition of Au^0 for the formation of GNSs, eventually producing gold nanostructures with rounded tips or no tips observed with respect to PVP-10. However, the too weak reducing power of PVP-8 is unable to produce the GNS structure. Thus, these results clearly demonstrate the dramatic influence of the PVP molecular weight on the morphology of GNSs in the seed-mediated synthesis.

We further examined the effect of the PVP concentration using PVP-10 because its use produced high-quality GNSs (Figure 2). These GNSs from different PVP-10 concentrations exhibit similar extinction spectra with slight spectral broadening and main plasmon band shifting, except the GNSs synthesized at the concentration of 2.0 mM. The main plasmon wavelength first red-shifts and then blue-shifts with increasing PVP concentration. TEM images clearly show the GNS structures of five protruding tips. The core size has little dependence on the PVP concentration, and the tip length is the biggest at the concentration of 5.0 mM (Figures 2C and S3). We also observed the growth of subbranches at the high PVP-10 concentration of 20.0 mM, similar to our previous observation with the high Au^{3+}/gold seed ratio for the growth of GNSs.[9]

To better understand the structural evolution of GNSs and their morphology−plasmonic property relationships, we performed FDTD simulations with the geometrical model created using the dimensional parameters statistically obtained from the TEM images (Table 1 and Figures S2−S4). Figure 3A presents the calculated extinction spectra of the gold core, assembly of five protruding tips without a core, and GNS. It can be clearly seen that the gold core and the assembly of five protruding tips exhibit their main plasmon peaks at 528 and 688 nm, respectively. The calculated extinction spectrum of

Table 1. Summary of Synthetic Conditions of GNSs in This Work and Their Structural Dimensions Statistically Obtained from the TEM Data

sample	temp (°C)	[PVP] (mM)	PVP MW	core size (nm)	tip length (nm)	tip no.[a]
1	25	5.0	10K	25.10 ± 2.76	16.11 ± 3.94	5
2	25	5.0	24K	29.19 ± 3.64	11.16 ± 5.35	NA
3	25	5.0	40K	33.32 ± 4.03	14.54 ± 3.52	5
4	25	5.0	58K	28.26 ± 4.22	7.78 ± 3.98	NA
5	25	2.0	10K	27.31 ± 3.00	12.12 ± 3.83	5
6	25	2.5	10K	24.56 ± 3.45	14.11 ± 5.14	5
7	25	10.0	10K	26.08 ± 3.27	14.26 ± 3.61	5
8	25	20.0	10K	26.14 ± 3.20	13.01 ± 3.20	5
9	0	5.0	10K	25.72 ± 4.11	10.80 ± 3.00	5
10	100	5.0	10K	29.28 ± 2.52	9.01 ± 3.00	NA

[a]NA means not available. This is because of the absence of the protruding tips or the too short tip length.

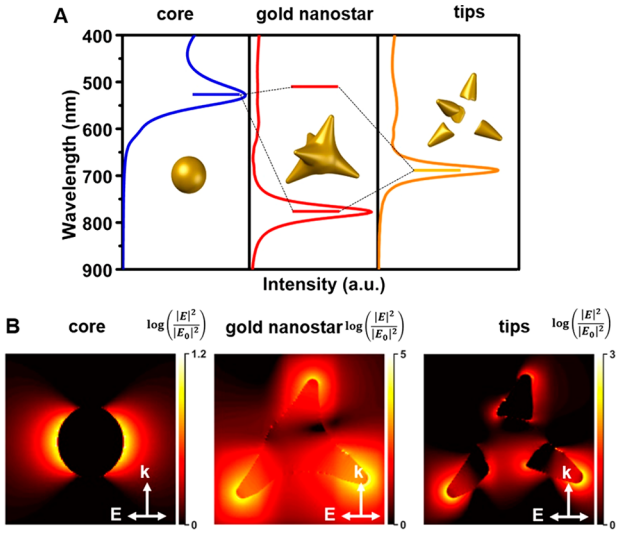

Figure 3. Plasmon hybridization modeling for GNSs. (A) Calculated extinction spectra and (B) normalized electric field ($|E|^2/|E_0|^2$) distribution at 785 nm of the gold core, the assembly of five-protruding tips without the core, and a single GNS consisting of a central core and five protruding tips uniformly distributed on the central core. The size of the gold core and dimensional parameters/distribution of five protruding tips are consistent with those in the GNS. All of these dimensional parameters for the FDTD simulations are from the GNS sample synthesized using 5.0 mM PVP-10 at 25 °C, statistically obtained from the TEM data in Figure 1C(i). The energy levels of the plasmon modes and corresponding geometrical models of the gold core, five-protruding-tip assembly, and GNS for the FDTD simulations are shown as well in part A.

GNSs shows a weak plasmon peak at 520 nm and a strong plasmon peak at 777 nm, which is in very good agreement with the experimental one (Figure 1B). The two plasmon bands of GNSs can be explained by hybridization of the core and tip dipolar plasmon modes.[9,10] The normalized local electric field intensity ($|E|^2/|E_0|^2$) with respect to the 785 nm incident field in the absence of gold nanostructures is shown in Figure 3B. We can clearly see that the maximum $|E|^2/|E_0|^2$ of GNSs is 2 and 4 orders of magnitude higher than those of the five-tip assembly and gold core, respectively. The nonlinear hybridization between plasmons associated the central core and tip assembly yields a large molar extinction coefficient of 2.1×10^{10} M^{-1} cm^{-1} at a resonance wavelength of 777 nm, significantly higher than 1.7×10^9 M^{-1} cm^{-1} of the core and 3.9×10^9 M^{-1} cm^{-1} of the tip assembly at their respective plasmon wavelengths (Figure S5).

Considering the complicated geometry of GNSs, we further explored the influence of the number of protruding tips on the plasmonic response and electric-field distribution using the same core and tip geometries aforementioned without any further adjustments except the number of protruding tips (Figure 4). FDTD simulations predict that the main plasmon peak red-shifts from 528 nm of the gold core to 741 and 777 nm when one and two protruding tips are on the core, respectively (Figure 4A). Surprisingly, we find that the plasmon wavelength remains constant at 777 nm but its extinction intensity increases with a further increase of the number of protruding tips on the core from two to five. This indicates that the geometrical model created here for FDTD simulations can very well reflect the real geometry of the synthesized GNSs with uniform distribution of five protruding

DOI: 10.1021/acs.inorgchem.9b02187
Inorg. Chem. XXXX, XXX, XXX−XXX

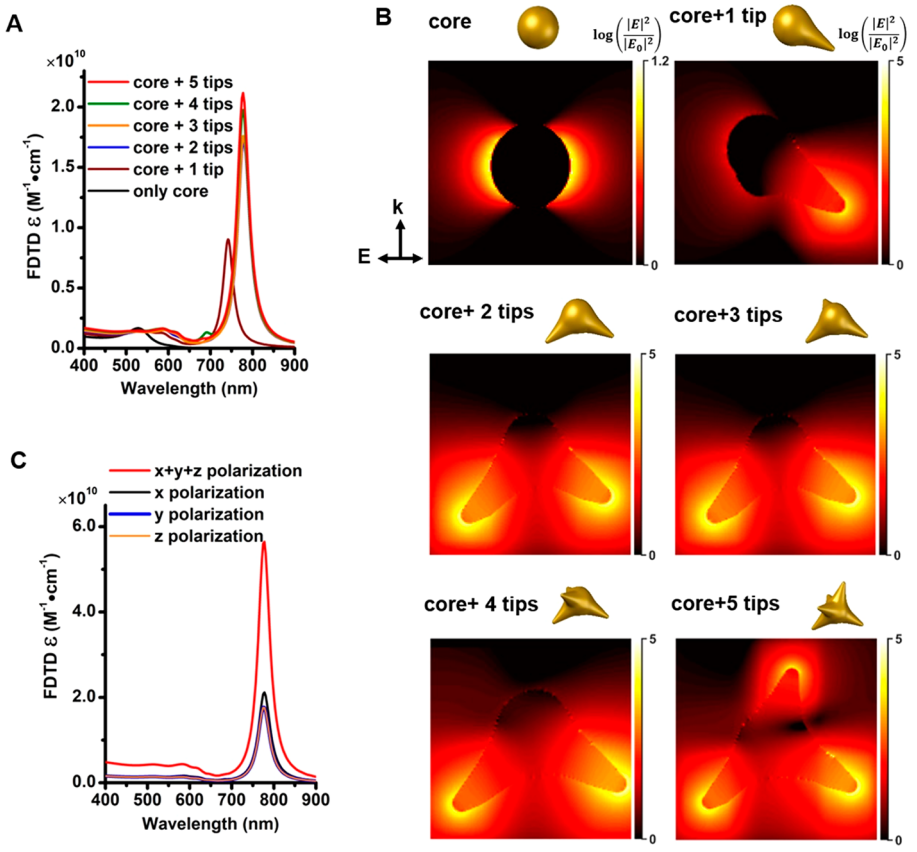

Figure 4. Effect of the number of the protruding tips and polarization direction of incident light on the plasmonic response of the GNSs. (A) Calculated extinction spectra and (B) normalized electric-field ($|E|^2/|E_0|^2$) distribution excited at 785 nm of gold nanostructures containing a core and one to five protruding tips. (C) Calculated extinction spectra under *x*-, *y*-, or *z*-polarized incident light and summarized extinction spectrum of a single GNS. The size of the gold core and dimensional parameters/distribution of five protruding tips are from the GNS synthesized using 5.0 mM PVP-10 at 25 °C, statistically obtained from the TEM data in Figure 1C(i). The models for FDTD simulations are shown as well.

tips. The plasmonic core containing a single protruding tip behaves like a gold nanorod of high aspect ratio, leading to the red-shift of its plasmon band compared with that of the core. The same explanation can also be employed for the structure of a central core and two protruding tips. However, there exists a weak plasmonic coupling between these tips due to the large separation distance so that a further increase beyond two protruding tips could not further red-shift the plasmon wavelength. We found that the molar extinction coefficient (or extinction cross section) increases with the increasing number of protruding tips on the core (Figure S6). As expected, the electric-field intensity of the GNS increases with the increasing number of protruding tips (Figure 4B). We also examined the extinction spectra of GNSs under the *x*, *y*, or *z* polarization direction (Figure 4C). No additional plasmon mode was observed with respect to the polarization direction of the incident light. Our results corroborate that each plasmon mode in the extinction spectrum of GNSs is associated with one individual tip and the plasmonic coupling between their protruding tips is negligible. Although we are currently unable to experimentally make the GNSs with different tip numbers using the seed-mediated synthetic method, the theoretical analysis strengthens our understanding of the effect of the plasmonic properties of the tip number on the GNS. FDTD-calculated extinction spectra showed change trends consistent with the experimental ones, indicating the correct geometrical model for FDTD simulations (Figure 2A).

3.2. Effect of the Synthesis Temperature. To address the effect of the synthesis temperature on the seed-mediated growth of GNSs, we further monitored the growth of GNSs at different temperatures ranging from 0 to 100 °C in the presence of 5.0 mM PVP-10 (Figure 5). Similar extinction spectra were observed except a slight blue-shift and spectral broadening of plasmon bands at 0 °C with respect to those at 25 °C. The intensity of the main plasmon band at the long wavelength gradually weakens with increasing synthesis temperature from 40 to 100 °C, and eventually the short-wavelength plasmon band becomes dominant for the GNSs synthesized at 100 °C. TEM images reveal that the GNSs synthesized at 0 °C have a core size (25.72 ± 4.11 nm) similar to that (25.10 ± 2.76 nm) of GNSs synthesized at 25 °C but its tip length (10.80 ± 3.00 nm) is much smaller than that (16.11 ± 3.94 nm) of GNSs synthesized at 25 °C. However, the GNSs become rounded at 100 °C with fewer and shorter protruding tips because of the surface melting effect at high temperatures, widely reported for noble metallic nanostructures in the previous literature.[42,43] The surface melting effect and resultant reshaping of GNSs were further confirmed by the time-dependent blue shift of the dominant plasmon band of the GNS colloids by heating at 90 °C (Figure S7). The temperature-induced structural change causes the main plasmon wavelength to first red-shift from 731 to 781 nm from 0 to 25 °C and then blue-shift to 550 nm as the temperature increases to 100 °C. The GNSs synthesized at 25 °C have the smallest core size and biggest tip length, while the

DOI: 10.1021/acs.inorgchem.9b02187
Inorg. Chem. XXXX, XXX, XXX−XXX

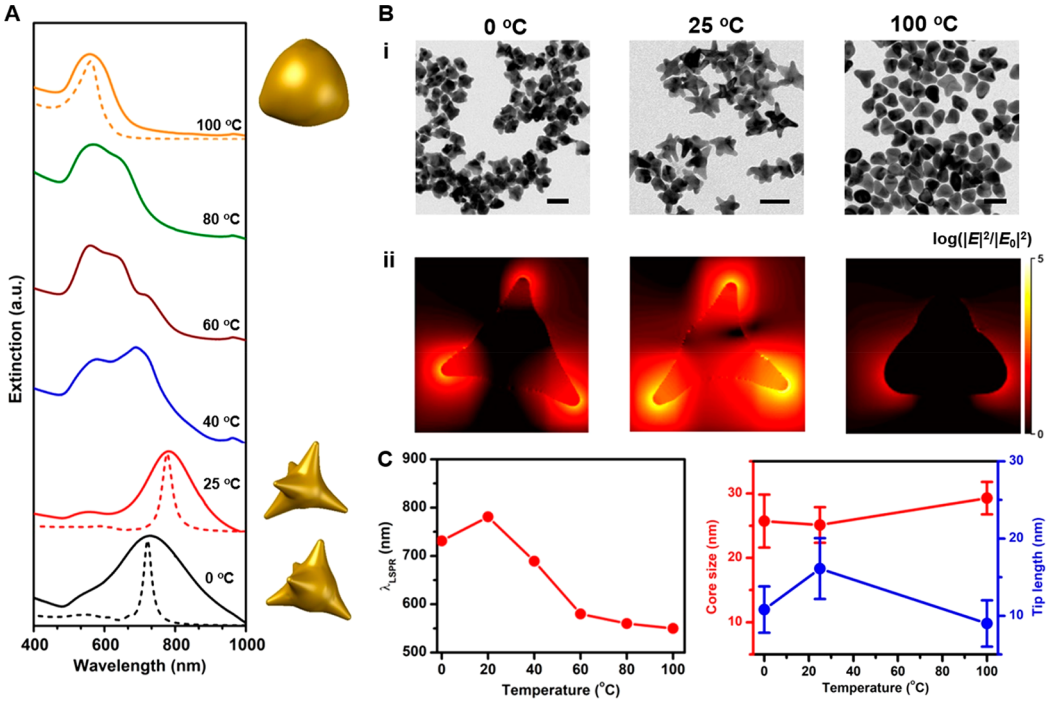

Figure 5. Effect of the synthesis temperature on the structure and plasmonic properties of GNSs. (A) Experimental (solid line) and calculated (short dotted line) extinction spectra of GNSs synthesized at various temperatures (0, 25, 40, 60, 80, and 100 °C). The geometrical models used for FDTD simulations are shown as well. (B) Representative TEM images and normalized electric-field ($|E|^2/|E_0|^2$) distribution excited at 785 nm of GNSs synthesized at 0, 25, and 100 °C. (C) (i) Plasmon wavelength and (ii) core size and tip length of GNSs as a function of the synthesis temperature.

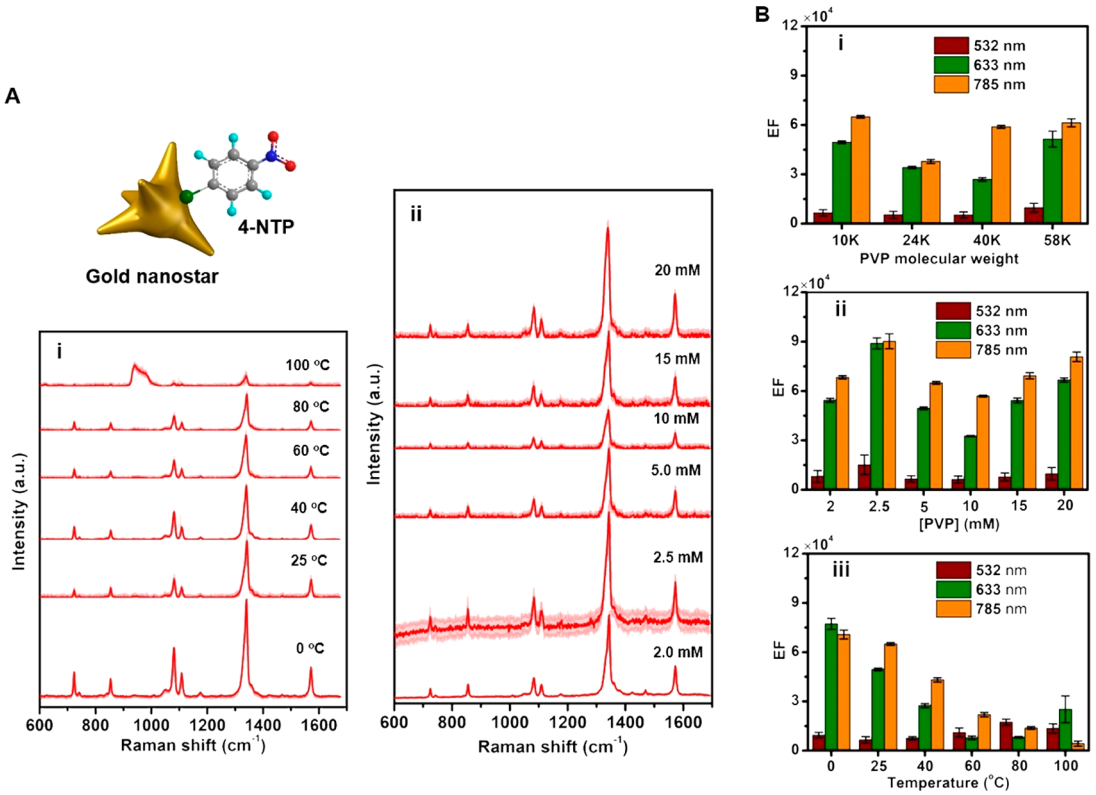

Figure 6. SERS performance of GNSs synthesized under varying synthesis conditions. (A) SERS spectra at the 785 nm excitation wavelength of GNSs synthesized at (i) varying synthesis temperatures (0, 25, 40, 60, 80, and 100 °C) in the presence of 5.0 mM PVP-10 and (ii) varying PVP-10 concentrations (2.0, 2.5, 5.0, 10.0, 15.0, and 20.0 mM) at 25 °C. A schematic model of 4-NTP-modified GNSs is shown as well. (B) SERS EFs at the 532, 633, or 785 nm excitation wavelength of GNSs synthesized with (i) 5.0 mM PVP of various molecular weights at 25 °C, (ii) various PVP-10 concentrations at 25 °C, and (iii) various synthesis temperatures in the presence of 5.0 mM PVP-10.

DOI: 10.1021/acs.inorgchem.9b02187
Inorg. Chem. XXXX, XXX, XXX−XXX

biggest core size and smallest tip length are achieved at 100 °C [Figure 5C(ii)]. All of these results substantiate that the synthesis temperature must be carefully considered for the seed-mediated synthesis of GNSs. FDTD simulations of GNSs using dimensional parameters extracted from the TEM data produced extinction spectra consistent with the experimental ones, except the distinct spectral width due to the simplified FDTD model and the polydispersity of synthesized GNSs (Figure 5A,B). FDTD simulations also show that the higher synthesis temperature results in a less intense plasmon band and low electric-field enhancement, which is attributed to the rounded protruding tips [Figure 5B(ii)].

3.3. Structure-Dependent SERS Enhancement. To reveal the influence of structures on the SERS enhancement of the GNSs, we performed the SERS measurements using 4-NTP as the Raman molecules at three different excitation wavelengths of 532, 633, and 785 nm (Figure 6). GNSs were immersed in an aqueous solution containing 4-NTP molecules, followed by washing with ultrapure water to remove excess 4-NTP molecules. The average number of Raman molecules adsorbed on a single GNS is determined according to UV−vis extinction spectroscopy, whose details can be found in the Supporting Information. All of the detected Raman bands are in good agreement with the reported SERS spectra of 4-NTP.[11,31,32] The intense SERS bands around 1571, 1340, and 1078 cm^{-1} can be attributed to the C−C, O−N−O, and C−S stretching vibrations, respectively; the SERS bands at 1111 and 855 cm^{-1} can be attributed to the C−H bending and C−H wagging vibrations, respectively; the 723 cm^{-1} band can be related to the C−H, C−S, and C−C wagging vibrations.[11,31,32] Figure 6A confirmed the variations of the SERS intensity as a function of both the synthesis temperature and PVP concentration. The results indicate that the SERS intensity decreases with increasing synthesis temperature, as expected. This is because the high synthesis temperature leads to the rounded protruding tips and, consequently, decreases the local electric-field enhancement. Nevertheless, a nonmonotonous correlation was observed between the SERS intensity and PVP-10 concentration; the SERS intensity reaches a maximum at a PVP-10 concentration of 2.5 mM and a minimum at 10.0 mM PVP-10. We quantified the SERS performance through the SERS EF at the 532, 633, and 785 nm excitation wavelengths, respectively (Figure 6B). For GNSs synthesized with various PVP molecular weights, the SERS EFs are the highest at the 785 nm excitation wavelength and the lowest at the 532 nm excitation wavelength. Similarly, GNSs synthesized with different PVP-10 concentrations show much higher SERS EFs at the 633 and 785 nm excitation wavelengths than at the 532 nm excitation wavelength. The highest EF of 8.8×10^4 can be achieved at the PVP-10 concentration of 2.5 mM with the 785 nm excitation wavelength. Our results reveal that the SERS EFs at either 633 or 785 nm excitation wavelength dramatically decrease with increasing synthesis temperature, while the SERS EFs with 532 nm laser excitation slightly increase with the synthesis temperature.

Given the multiple sharp tips in the geometry of GNSs, the maximum local electric-field enhancement occurs in the vicinity of the sharp tips of the GNSs. A better resonance overlap of the plasmon band of the GNSs with the excitation wavelength would achieve a much higher SERS EF. The aforementioned results show the morphology, plasmonic properties, and SERS performance of GNSs as a function of the PVP molecular weight, its concentration, and synthesis temperature. Our FDTD simulations demonstrated more than 9 orders of magnitude SERS enhancement ($|E|^4/|E_0|^4$) at the apex of the protruding tips of the GNSs (Figures 3 and 4). The reducing power of the PVP molecules kinetically controls the anisotropic growth of GNSs. PVP-10 of a mild reducing power produces high-quality GNSs of sharp protruding tips, while PVP oligomers of high molecular weight such as PVP-24, PVP-40, and PVP-58 produce GNSs with rounded or short protruding tips due to the intertwined effects of the reducing power and steric hindrance of PVP. In addition, the morphology and plasmonic properties of GNSs are affected by the PVP concentration. The core size has little dependence on the PVP concentration, but the tip grows to the longest value at a PVP-10 concentration of 5.0 mM. The low synthesis temperature allows the growth of GNSs, while the high temperature results in the formation of rounded GNSs due to the surface melting effect. Thus, the SERS enhancement excited at the 633 or 785 nm laser decreases with the synthesis temperature due to the decreasing overlap of the plasmon band with the incident excitation wavelength, while the SERS enhancement at 532 nm slightly increases with the synthesis temperature due to the increasing extinction cross section with the particulate size. Therefore, we reveal that the dimensional parameters, including the core size and tip length of GNSs, can be tailored by changing the synthesis conditions, e.g., the PVP molecular weight, PVP concentration, and synthesis temperature. This work provides a paradigm for correlating the morphology with the plasmonic properties and clarifying the effects of multiparameters on the morphological evolution of GNSs by combining experimental investigations and FDTD simulations.

4. CONCLUSIONS

In summary, a combined strategy of experimental investigations and FDTD-based theoretical modeling has been exploited to elucidate the effects on the morphology of GNSs of multiple synthesis conditions (i.e., the PVP molecular weight, PVP concentration, and synthesis temperature) in the seed-mediated synthesis. We demonstrated the dramatic influence of the PVP molecular weight on both the core size and tip length of GNSs. PVP-10 of mild reducing power produces high-quality GNSs with long, sharp protruding tips, while PVP oligomers of high molecular weight such as PVP-24, PVP-40, and PVP-58 produce GNSs with rounded or short protruding tips. The tip length of GNSs first increases and then decreases with the PVP concentration, but little dependence of the core size on the PVP concentration is observed. The synthesis temperature dramatically affects the morphology of GNSs as well. FDTD simulations show the maximum local electric field enhancement at the apex of GNSs and demonstrate nonlinear hybridization of the core- and protruding-tip-associated plasmons in the extinction spectrum of GNSs. Negligible plasmonic coupling between the protruding tips is substantiated because of their large separation distance so that a further increase beyond two protruding tips only increases the extinction cross section without further red-shifting the plasmon wavelength. The morphological change of GNSs could modify the optical properties and thereby significantly affect the SERS enhancement. Effects of these synthesis conditions on the SERS EF vary with the incident laser wavelength, and an increasing resonance overlap of the plasmon band with the incident laser wavelength would produce a high SERS EF. The present work

DOI: 10.1021/acs.inorgchem.9b02187
Inorg. Chem. XXXX, XXX, XXX−XXX

clearly clarifies the critical influential factors of the seed-mediated synthesis of GNSs and strengthens our understanding on the growth of GNSs. More importantly, the FDTD simulations along with the experimental investigations allow correlations of the reaction-condition-dependent dimensional parameters with the plasmonic properties, which is unachievable by experiments alone. In this work, FDTD simulations along with the experimental investigations provide new scientific insights into the seed-mediated growth of GNSs and satisfactorily correlate their morphology−plasmonic properties. This study presents a paradigm for understanding the growth process of nanostructures and predicting their plasmonic properties by combining experiments and theoretical modeling.

■ ASSOCIATED CONTENT

Supporting Information

The Supporting Information is available free of charge on the ACS Publications website at DOI: 10.1021/acs.inorgchem.9b02187.

Calculation of the number of adsorbed Raman molecules, schematic geometry of a GNS, core-size and tip-length distributions of GNSs synthesized under varying synthesis conditions, FDTD-calculated molar extinction coefficients of the central core, assembly of five protruding tips, and GNSs, FDTD-calculated molar extinction coefficient of the gold core with protruding tips as a function of the number of protruding tips, and time-resolved extinction spectra of the GNS aqueous solution heated at 90 °C (PDF)

■ AUTHOR INFORMATION

Corresponding Author

*E-mail: liming0823@csu.edu.cn or liming0823@gmail.com. Web site: www.ming-group.com.

ORCID

Ming Li: 0000-0002-2289-0222

Author Contributions

†H.W. and Y.P. contributed equally to this work.

Notes

The authors declare no competing financial interest.

■ ACKNOWLEDGMENTS

M.L. acknowledges financial support by the National Thousand Young Talents Program of China, National Natural Science Foundation of China (Grant 51871246), Innovation-Driven Project of Central South University (Grant 2018CX002), and Hunan Provincial Science & Technology Program (Grant 2017XK2027).

■ REFERENCES

(1) Yuan, H.; Fales, A. M.; Vo-Dinh, T. TAT peptide-functionalized gold nanostars: enhanced intracellular delivery and efficient NIR photothermal therapy using ultralow irradiance. *J. Am. Chem. Soc.* **2012**, *134*, 11358−11361.

(2) Shan, B.; Pu, Y.; Chen, Y.; Liao, M.; Li, M. Novel SERS labels: Rational design, functional integration and biomedical applications. *Coord. Chem. Rev.* **2018**, *371*, 11−37.

(3) Nehl, C. L.; Liao, H.; Hafner, J. H. Optical properties of star-shaped gold nanoparticles. *Nano Lett.* **2006**, *6*, 683−688.

(4) Li, M.; Cushing, S. K.; Wu, N. Plasmon-enhanced optical sensors: a review. *Analyst* **2015**, *140*, 386−406.

(5) Li, M.; Cushing, S. K.; Zhang, J.; Lankford, J.; Aguilar, Z. P.; Ma, D.; Wu, N. Shape-dependent surface-enhanced Raman scattering in gold−Raman-probe−silica sandwiched nanoparticles for biocompatible applications. *Nanotechnology* **2012**, *23*, 115501.

(6) Halas, N. J.; Lal, S.; Chang, W. S.; Link, S.; Nordlander, P. Plasmons in strongly coupled metallic nanostructures. *Chem. Rev.* **2011**, *111*, 3913−3961.

(7) Yang, P.; Zheng, J.; Xu, Y.; Zhang, Q.; Jiang, L. Colloidal synthesis and applications of plasmonic metal nanoparticles. *Adv. Mater.* **2016**, *28*, 10508−10517.

(8) Yang, X.; Yang, M.; Pang, B.; Vara, M.; Xia, Y. Gold nanomaterials at work in biomedicine. *Chem. Rev.* **2015**, *115*, 10410−10488.

(9) Pu, Y.; Zhao, Y.; Zheng, P.; Li, M. Elucidating the growth mechanism of plasmonic gold nanostars with tunable optical and photothermal properties. *Inorg. Chem.* **2018**, *57*, 8599−8607.

(10) Hao, F.; Nehl, C. L.; Hafner, J. H.; Nordlander, P. Plasmon resonances of a gold nanostar. *Nano Lett.* **2007**, *7*, 729−732.

(11) Li, M.; Kang, J. W.; Dasari, R. R.; Barman, I. shedding light on the extinction-enhancement duality in gold nanostar-enhanced Raman spectroscopy. *Angew. Chem., Int. Ed.* **2014**, *53*, 14115−14119.

(12) Sau, T. K.; Rogach, A. L.; Döblinger, M.; Feldmann, J. One-step high-yield aqueous synthesis of size-tunable multispiked gold nanoparticles. *Small* **2011**, *7*, 2188−2194.

(13) Khoury, C. G.; Vo-Dinh, T. Gold nanostars for surface-enhanced Raman scattering: synthesis, characterization and optimization. *J. Phys. Chem. C* **2008**, *112*, 18849−18859.

(14) Yamamoto, M.; Kashiwagi, Y.; Sakata, T.; Mori, H.; Nakamoto, M. Synthesis and morphology of star-shaped gold nanoplates protected by poly (N-vinyl-2-pyrrolidone). *Chem. Mater.* **2005**, *17*, 5391−5393.

(15) Moukarzel, W.; Fitremann, J.; Marty, J. D. Seedless amino-sugar mediated synthesis of gold nanostars. *Nanoscale* **2011**, *3*, 3285−3290.

(16) Senthil Kumar, P.; Pastoriza-Santos, I.; Rodriguez-Gonzalez, B.; Javier García de Abajo, F.; Liz-Marzan, L. M. High-yield synthesis and optical response of gold nanostars. *Nanotechnology* **2008**, *19*, 015606.

(17) Wu, H. L.; Chen, C. H.; Huang, M. H. Seed-mediated synthesis of branched gold nanocrystals derived from the side growth of pentagonal bipyramids and the formation of gold nanostars. *Chem. Mater.* **2009**, *21*, 110−114.

(18) Liu, X. L.; Wang, J. H.; Liang, S.; Yang, D. J.; Nan, F.; Ding, S. J.; Zhou, L.; Hao, Z. H.; Wang, Q. Q. Tuning plasmon resonance of gold nanostars for enhancements of nonlinear optical response and Raman scattering. *J. Phys. Chem. C* **2014**, *118*, 9659−9664.

(19) Niu, W.; Chua, Y. A. A.; Zhang, W.; Huang, H.; Lu, X. Highly symmetric gold nanostars: crystallographic control and surface-enhanced Raman scattering property. *J. Am. Chem. Soc.* **2015**, *137*, 10460−10463.

(20) Li, M.; Zhang, J.; Suri, S.; Sooter, L. J.; Ma, D.; Wu, N. Detection of adenosine triphosphate with an aptamer biosensor based on surface-enhanced Raman scattering. *Anal. Chem.* **2012**, *84*, 2837−2842.

(21) Koczkur, K. M.; Mourdikoudis, S.; Polavarapu, L.; Skrabalak, S. E. Polyvinylpyrrolidone (PVP) in nanoparticle synthesis. *Dalton Trans.* **2015**, *44*, 17883−17905.

(22) Pastoriza-Santos, I.; Liz-Marzán, L. M. Formation of PVP-protected metal nanoparticles in DMF. *Langmuir* **2002**, *18*, 2888−2894.

(23) Kyrychenko, A.; Korsun, O. M.; Gubin, I. I.; Kovalenko, S. M.; Kalugin, O. N. Atomistic simulations of coating of silver nanoparticles with poly (vinylpyrrolidone) oligomers: Effect of oligomer chain length. *J. Phys. Chem. C* **2015**, *119*, 7888−7899.

(24) Zou, X.; Ying, E.; Dong, S. Seed-mediated synthesis of branched gold nanoparticles with the assistance of citrate and their surface-enhanced Raman scattering properties. *Nanotechnology* **2006**, *17*, 4758.

(25) Osinkina, L.; Lohmuller, T.; Jackel, F.; Feldmann, J. Synthesis of gold nanostar arrays as reliable, large-scale, homogeneous

DOI: 10.1021/acs.inorgchem.9b02187
Inorg. Chem. XXXX, XXX, XXX−XXX

substrates for surface-enhanced Raman scattering imaging and spectroscopy. *J. Phys. Chem. C* **2013**, *117*, 22198−22202.
(26) Yamamoto, M.; Kashiwagi, Y.; Sakata, T.; Mori, H.; Nakamoto, M. Synthesis and morphology of star-shaped gold nanoplates protected by poly (N-vinyl-2-pyrrolidone). *Chem. Mater.* **2005**, *17*, 5391−5393.
(27) Xie, J.; Zhang, Q.; Lee, J. Y.; Wang, D. I. The synthesis of SERS-active gold nanoflower tags for in vivo applications. *ACS Nano* **2008**, *2*, 2473−2480.
(28) Maiorano, G.; Rizzello, L.; Malvindi, M. A.; Shankar, S. S.; Martiradonna, L.; Falqui, A.; Cingolani, R.; Pompa, P. P. Monodispersed and size-controlled multibranched gold nanoparticles with nanoscale tuning of surface morphology. *Nanoscale* **2011**, *3*, 2227−2232.
(29) Li, M.; Cushing, S. K.; Zhang, J.; Suri, S.; Evans, R.; Petros, W. P.; Gibson, L. F.; Ma, D.; Liu, Y.; Wu, N. Three-dimensional hierarchical plasmonic nano-architecture enhanced surface-enhanced Raman scattering immunosensor for cancer biomarker detection in blood plasma. *ACS Nano* **2013**, *7*, 4967−4976.
(30) Jin, Q.; Li, M.; Polat, B.; Paidi, S. K.; Dai, A.; Zhang, A.; Pagaduan, J. V.; Barman, I.; Gracias, D. H. Mechanical Trap Surface-Enhanced Raman Spectroscopy for Three-Dimensional Surface Molecular Imaging of Single Live Cells. *Angew. Chem., Int. Ed.* **2017**, *56*, 3822−3826.
(31) Li, M.; Kang, J. W.; Sukumar, S.; Dasari, R. R.; Barman, I. Multiplexed detection of serological cancer markers with plasmon-enhanced Raman spectro-immunoassay. *Chem. Sci.* **2015**, *6*, 3906−3914.
(32) Li, M.; Banerjee, S. R.; Zheng, C.; Pomper, M. G.; Barman, I. Ultrahigh affinity Raman probe for targeted live cell imaging of prostate cancer. *Chem. Sci.* **2016**, *7*, 6779−6785.
(33) Li, L.; Liao, M.; Chen, Y.; Shan, B.; Li, M. Surface-Enhanced Raman Spectroscopy (SERS) Nanoprobes for Ratiometric Detection of Cancer Cells. *J. Mater. Chem. B* **2019**, *7* (5), 815−822.
(34) Le Ru, E.; Etchegoin, P. *Principles of Surface-Enhanced Raman Spectroscopy: And Related Plasmonic Effects*; Elsevier: Amsterdam, The Netherlands, 2008.
(35) Orendorff, C. J.; Gole, A.; Sau, T. K.; Murphy, C. J. Surface-enhanced Raman spectroscopy of self-assembled monolayers: sandwich architecture and nanoparticle shape dependence. *Anal. Chem.* **2005**, *77*, 3261−3266.
(36) Johnson, P. B.; Christy, R. W. Optical constants of the noble metals. *Phys. Rev. B* **1972**, *6*, 4370.
(37) Navarro, J. R.; Werts, M. H. Resonant light scattering spectroscopy of gold, silver and gold−silver alloy nanoparticles and optical detection in microfluidic channels. *Analyst* **2013**, *138*, 583−592.
(38) Barbosa, S.; Agrawal, A.; Rodríguez-Lorenzo, L.; Pastoriza-Santos, I.; Alvarez-Puebla, R. A.; Kornowski, A.; Weller, H.; Liz-Marzán, L. M. Tuning size and sensing properties in colloidal gold nanostars. *Langmuir* **2010**, *26*, 14943−14950.
(39) Washio, I.; Xiong, Y.; Yin, Y.; Xia, Y. Reduction by the end groups of poly (vinyl pyrrolidone): a new and versatile route to the kinetically controlled synthesis of Ag triangular nanoplates. *Adv. Mater.* **2006**, *18*, 1745−1749.
(40) Chou, K. S.; Lai, Y. S. Effect of polyvinyl pyrrolidone molecular weights on the formation of nanosized silver colloids. *Mater. Chem. Phys.* **2004**, *83*, 82−88.
(41) Song, Y. J.; Wang, M.; Zhang, X. Y.; Wu, J. Y.; Zhang, T. Investigation on the role of the molecular weight of polyvinyl pyrrolidone in the shape control of high-yield silver nanospheres and nanowires. *Nanoscale Res. Lett.* **2014**, *9*, 17.
(42) Gocyla, M.; Kuehl, S.; Shviro, M.; Heyen, H.; Selve, S.; Dunin-Borkowski, R. E.; Heggen, M.; Strasser, P. Shape stability of octahedral Pt-Ni nanocatalysts for electrochemical oxygen reduction reaction studied by in situ transmission electron microscopy. *ACS Nano* **2018**, *12*, 5306−5311.
(43) Rahman, D. S.; Chatterjee, H.; Ghosh, S. K. Excess surface energy at the tips of gold nanospikes: from experiment to modeling. *J. Phys. Chem. C* **2015**, *119*, 14326−14337.

DOI: 10.1021/acs.inorgchem.9b02187
Inorg. Chem. XXXX, XXX, XXX−XXX